Supplementary Materials for

Wood Ice Seed for Sea Ice Generation

Table of content

Part III: Supplementary Tables

Supplementary Discussions

Supplementary Discussion 1. Ice-Wood preparation

S1.1 Wood delignification and carbonization

A natural basswood (*Tilia Americana*) block of 10x10x1.5 cm^3 (longitudinal x tangential x radial) was cut into two pieces, where a 2.5x2.5x1.5 cm^3 piece was cut from the center of the basswood block for carbonization and the remaining is delignified. The smaller centerpiece was carbonized on one longitudinal side by contacting a 350 °C hotplate for 45 s. The other piece was kept in a sealed glass container of 250 mL 30% H_2O_2 solution and heated with a hotplate at 80 °C for 24 hours. The delignified wood was soak-washed with DI water twice and naturally dried in a fume hood for 48 hours. H_2O_2 was reported to have 1 hour to 10 days of aquatic half-lives and presented no bioaccumulation[1]. For any possible remaining H_2O_2 in Ice-Wood deployment, we expected a minimal increase of H_2O_2 concentration in the ocean and thereby no ecotoxicity risk.

S1.2 Ice-Wood assembly

The Ice-Wood can be assembled with separately functionalized pieces and a transparent umbrella frame for condensation and water redirection. The skeleton of the condensation umbrella was made of a clear acrylic square tube of 2.5x2.5x1.0 cm^3 and acrylic rods of 1/8 inches (3.175 mm) diameter attached with acrylic cement. A LDPE film (~10-μm thickness) with high infrared (IR) transparency covered the skeleton to complete the condensation umbrella. The carbonized center wood was assembled into the delignified wood, and the condensation umbrella was glued to the carbonized center wood.

S1.3 Potential large-scale fabrication

A large wood block can be top delignified by spraying H_2O_2 and exposed to UV light or natural sunlight. The longitudinal pathway is the dominant carrier of water, nutrients, and waste between the top of the canopy down to the root as the result of natural selection of plant growth direction. Such anisotropic fluidic transport behavior is desirable for one-sided surface functionalization for our selected sample orientation as the H_2O_2 solution can spread faster across the surface than into it. Then, energy and chemicals can be greatly reduced for a large-scale Ice-Wood fabrication with similar surface functionalization. Some wood portions at the designated area ratio will be cut out before the delignification, undergo carbonization, and are assembled back to the large top-delignified wood.

Supplementary Discussion 2. Monte Carlo simulation of optical constants and properties

To further investigate the structure-optics interaction in natural and delignified wood, we employ Monte Carlo simulations to illuminate the spectral response. These simulations offer valuable insights into the photon behavior within functionalized wood materials. We assume the material system is composed of air pores and a wood matrix. Specifically, the air pores act as scattering centers for incident photons for reflections, while the wood matrix serves as an absorbing medium comprising a homogenous mixture of cellulose, hemicellulose, and lignin. We assume the hemicellulose has identical optical constants with cellulose in the modeling[2].

The first step is determining the spectral optical constants of materials. The refractive indexes (n) of cellulose and lignin are from Ref.[3,4] (Fig. S25). As the extinction coefficients (κ) of cellulose and lignin vary for different species of wood[5], they are determined by fitting the experimentally measured absorptance (Fig. 2c) with the gradient descent method. The fitted extinction coefficient of cellulose in the wood is nearly negligible in the visible range, similar to values in the literature[6,7]. The fitted extinction coefficient of lignin is also comparable with the reported value in the literature[3,8] (Fig. S26). For air, we consider the refractive index to be one and the extinction coefficient to be zero across the entire wavelength range in the simulation.

The spectral optical properties of natural and delignified wood matrices are subsequently calculated using the Maxwell-Garnett model[9]

$$\frac{\varepsilon_{\mathrm{EM}}-\varepsilon_{\mathrm{cellulose}}}{\varepsilon_{\mathrm{EM}}+2\varepsilon_{\mathrm{cellulose}}}=f_{\mathrm{lignin}}\frac{\varepsilon_{\mathrm{lignin}}-\varepsilon_{\mathrm{cellulose}}}{\varepsilon_{\mathrm{lignin}}+2\varepsilon_{\mathrm{cellulose}}} \quad (1)$$

where $\varepsilon_{\mathrm{EM}}$ is the effective permittivity of the wood matrix. f_{lignin} is the volume fraction of lignin in the natural wood and delignified wood from experiment[10]. $\varepsilon_{\mathrm{cellulose}}$ and $\varepsilon_{\mathrm{lignin}}$ are the permittivity of cellulose and lignin, respectively, which are derived from refractive index and extinction coefficient by

$$(n+i\kappa)^2=\varepsilon \quad (2)$$

The effective permittivity values of the delignified and natural wood matrices are then converted back into the refractive index and extinction coefficient for Monte Carlo simulation (Fig. S27).

The air pores are modeled as spherical scatterers within the system. Based on the measured porosity distribution of wood (Fig. S28), we select four representative diameters (d) of air pores (0.1 μm, 0.3 μm, 1 μm, 10 μm) and assume their corresponding volume fractions as 3%, 40%, 30%, 3% respectively, which sums up to the porosity of the wood matrix.

The scattering efficiency Q_{sca}, extinction efficiency Q_{ext}, absorption efficiency Q_{abs}, and asymmetry parameter g_{s} are given by[11-13]

$$Q_{\mathrm{sca}}=\frac{2}{x^2}\sum_{n=1}^{\infty}(2n+1)\left(|a_n|^2+|b_n|^2\right) \quad (3)$$

$$Q_{\text{ext}} = \frac{2}{x^2}\sum_{n=1}^{\infty}(2n+1)\,\text{Re}\{a_n + b_n\} \tag{4}$$

$$Q_{\text{abs}} = Q_{\text{ext}} - Q_{\text{sca}} \tag{5}$$

$$g_{\text{s}} = \frac{4}{x^2}\left[\sum_{n=1}^{\infty}\frac{n(n+2)}{n+1}\text{Re}\left(a_n a_{n+1}^{*} + b_n b_{n+1}^{*}\right) + \sum_{n=1}^{\infty}\frac{(2n+1)}{n(n+1)}\text{Re}\left(a_n b_n^{*}\right)\right] \tag{6}$$

where a_n and b_n are the Mie coefficients and x is the size parameter ($x = \pi d/\lambda$).

An effective medium is then constructed with scattering coefficient $\sigma_{s\lambda}$, absorption coefficient κ_λ, and asymmetry parameter of the effective medium g_λ given by

$$\sigma_{s\lambda} = \sum_{i=1}^{c}\frac{3f_i Q_{sca,i}}{2d_i},\ \kappa_\lambda = \sum_{i=1}^{c}\frac{3f_i Q_{abs,i}}{2d_i},\ g_\lambda = \frac{1}{\sigma_\lambda}\sum_{i=1}^{c}\frac{3f_i g_{s,i} Q_{sca,i}}{2d_i} \tag{7}$$

where f_i and d_i are the volume fraction and the diameter of corresponding air pores.

We also consider the dependent scattering effects and the distribution of diameters of air pores. A detailed introduction to building an effective medium is described in Ref.[11-13].

Monte Carlo simulations are then carried out to stochastically solve the radiation transport equation[12]. The simulation serves to accurately model the interaction of photons and scatterers within the medium. The medium is considered to have air as the upper and lower mediums sandwiching the wood matrix of thickness of 1 cm. The wavelength range covered in the simulation spans over the solar spectrum. 500,000 photons are released into the medium per wavelength. Each photon's trajectory and energy are tracked throughout its propagation within the medium, allowing the calculation of spectral reflectance, absorptance, and transmittance.

The simulated absorptances of natural and delignified wood achieve good agreement with the measured one in Fig. S29. The simulated total solar reflectance is 76.3% and 91.0% for natural and delignified wood, respectively, which are close to experimental data of 70.5% and 91.1%.

Supplementary Discussion 3. Material characterizations

SEM was taken by FEI Nova nanoSEM and analyzed by ImageJ. The characteristic length scale of vessels and pits are extracted from the SEMs and represented as the effective diameters in Fig. S5. For natural, delignified, and carbonized wood, their mean vessel diameters are 60.0-65.7 μm while the pit size slightly reduces after delignification or carbonization. The pore size distribution is characterized by a mercury intrusion porosimeter (Micromeritics AutoPore V).

The optical spectra between 250 – 2000 nm were measured by Perkin Elmer Lambda 950 UV-VIS-NIR spectrometer and IR spectra between 2 – 20 μm were measured by Nicolet iS50 FTIR spectrometer with a PIKE Technologies integrating sphere. The theoretical cooling power is calculated based on a previously reported method[14]. The thermal conductivities are measured by a steady-state hot-place method according to the ASTM standard.

Cyclic freezing and thawing: Basswood samples were cut to the specified dimensions (5x2x0.3 cm^3) and submerged in the 3.5% salt solution for 12 hours to simulate prolonged seawater exposure. After soaking, samples were removed from the salt solution, and excess liquid was drained. To simulate the frozen-drying cycle in the Arctic scenario, we placed the samples in a freezer set to -20 °C for 1 hour, ensuring they were fully frozen. After they froze, we transferred the samples to the room temperature environment (~20 °C) and allowed them to thaw completely until they reached room temperature. This completes one freeze-thaw cycle. This freeze-thaw cycle was repeated for 1, 10, 30, 50, 100, and 150 times for different sets of samples. Each set contains 5 samples. After completing the required number of cycles for each sample group, tensile tests were conducted on each sample with a tensile meter (MTS Criterion® Series 40 Electromechanical Universal Test Systems).

Supplementary Discussion 4. Fluidic transport analysis

S4.1 Capillary rise experiment

A strip of the natural basswood block was sliced by a razor blade along the radial direction. The vessels in the wood slice are perpendicular to the flow direction. The strip had a dimension of 0.2x0.5x1.5 cm^3 (longitudinal x tangential x radial). The capillary rising was filmed as the bottom of strip touched blue-dyed DI water with a known scale by caliper. The recorded video was analyzed by LoggerPro to extract the capillary rise height vs. time. A constant error of 0.5 mm is assigned to account for the uncertainty of manual point selection in the software.

Water molecules can diffuse within the solid cell walls and interact with the three major compositions of wood: cellulose, hemicelluloses, and lignin. Within nanoscale pores, the intermolecular potentials between the surfaces overlap leading to the physisorption of intermediate water. The physisorption allows more water-water interaction and further improves the surface wettability for capillary rise. The microstructures' capillary effect coupled with the high hydrophilicity leads to efficient microfluidic transport along the radial direction of Ice-Wood structure as shown in Fig. S30.

S4.2 Analytical model of mesoscopic water transport along radial-tangential direction

Mass transport is the other important aspect of the continuous ice growth and water-matter interaction[15] in the Ice-Wood. An analytical model derived by fitting the experimental capillary height reveals the relationship between the transport kinetics and the feature length of the microstructures as well as between the transport kinetics and surface hydrophilicity.

The mesoscopic water transport along the vessels of hardwood and tracheid of softwood along the longitudinal direction has been extensively studied[16-18]. Their behavior, in its simplest form, can be idealized as capillary rise along circular tubes described by Jurin's Law for equilibrium capillary height[19] and momentum balance for transient capillary rise[20]. However, the analytical model of mesoscopic transport behavior along the radial-tangential direction is scarce. It can be conceptualized as 1D microcapillary rise between two parallel plates with a periodic flow restriction imposed by the bordered pits (Fig. S31). The distance between the plates and the interval between bordered pits are both regarded as the effect diameter of vessels because they can be regarded as square cells. Since the diameter of bordered pits is one order of magnitude smaller than those of channels and vessels, the equilibrium capillary height (h_{eq}) is governed by the effective diameter of wood vessels (d_{vessel}). It can be determined by balancing the capillary pressure with hydrostatic pressure as

$$h_{eq} = \frac{2\gamma \cos(\theta)}{d_{vessel}\rho g} \tag{8}$$

where γ and ρ are the water's surface tension and density evaluated at 20 °C respectively. θ and g are the contact angle of the cell wall and gravitational acceleration respectively.

Knowing the h_{eq}, the experimentally measured capillary height as a function of time (t) can be nondimensionalized as

$$h^*(t) = \frac{h(t) - h_i}{h_{eq} - h_i} \tag{9}$$

where h_i is a non-zero initial height. The dimensionless variables like concentration, mass, and height describing the same physics are regarded as equal. Then, the diffusion coefficient of water (D_w) can be derived by fitting the following equation according to Ref.[21].

$$h^*(t) = \frac{4}{l}\sqrt{\frac{D_w}{\pi}} \cdot \sqrt{t} \tag{10}$$

where l is the sample length along the flow direction, i.e. the radial direction.

From Eq. (8)-(10), the fitted D_w depends on the vessel diameter and wood contact angle. The analytical solution of D_w between 1 – 100 μm vessel diameter at 63° contact angle for natural basswood[22], where the calculated D_w within the measured vessel diameter range agrees with the literature[21]. The mapping of h_{eq} vs. d_{vessel} vs. θ in Fig. S32a shows that larger vessel diameter and lower contact angle, i.e. greater hydrophilicity, leading to higher equilibrium height. h_{eq} exponentially decays with increasing d_{vessel} but parabolically decreases with increasing θ. Whereas the trend of D_w is inverse of that of h_{eq}. A larger vessel leads to greater water diffusion. Super hydrophobicity is favored in water diffusion as D_w increases exponentially with increasing θ (Fig. S32b). Increasing fluidic channel size and lowering surface hydrophilicity both reduce the equilibrium capillary height but enhance the mass diffusion coefficients. Thus, in the wood microstructure, the bordered pits and small channels exhibit high equilibrium capillary height that contributes to the high-water holding capacity (i.e. quantity), whereas the large vessels with high water diffusion coefficients accelerate the transport kinetics (i.e. speed).

S4.3 Solar steam generation experiment

A 2.5x2.5x1.5 cm carbonized wood was placed in a square container filled with DI water. The setup was placed on an analytic balance (Mettler Toledo XSR204) to record the mass change with a precision of 0.0001 g and an interval of 0.5 s. A solar simulator with Xenon Arc Lamp (UXL-150, Newport 67005) was used to induce solar-driven interfacial evaporation (Fig. S33). A thermocouple was attached to the side to monitor the temperature. The temperature data was collected by DAQ973A with the same time interval.

S4.4 Melt pond demonstration

In realistic melt ponds on top of carbonized wood, the water will evaporate while draining down. The same setup of the solar steam generation experiment was used for the melt pond drainage demonstration. A peptide quickly loaded DI water onto the top surface of carbonized wood without dripping from its sides to mimic the natural melt ponds. The step was repeated three times whenever DI water was completely drained. The discharge rate is calculated as the mass difference between the interval of water dripping.

Supplementary Discussion 5. Field validation test in ponds

The field validation of ice regeneration was conducted in open ponds between Jan. and Mar. 2024 at Purdue Aquaculture Research Center. Large-scale Ice-Wood samples were prepared from 10.16x91.44x1.59 cm^3 (4x36x0.625 in^3) wood planks to avoid the adhesives in the larger-sized feedstock. The wood underwent 30% H_2O_2 solution spraying followed by 24 hours of UV illumination twice. It was tied together by plastic wires to form the Ice-Wood sample. The plastic wires serve as a proof-of-concept manufacturing component and can be replaced with environmentally friendly alternatives. The carbonized portion was neglected in this field validation to primarily demonstrate the seeding effect. Two ponds were used as replicates. Each was virtually divided into two sections, an experiment group and a control group. The final size of Ice-Wood was 0.93x0.64 m^2, i.e. ~0.054% of the open area of the pond (~46x24 m^2). The sample was anchored to the center of the experimental group (the southern half of Pond 1 and the northern half of Pond 2). The temperature (± 0.5 °C by DJI Thermal Analysis Tool v3.2.1) and ice area (extracted by ImageJ, uncertainty ± 2%) were recorded by drones with digital and IR cameras (model DJI M3T). The ice thickness was manually measured by drilling holes in different locations with an uncertainty of 0.5 cm. The ambient conditions were recorded every 5 minutes by a weather station (Ambient weather WS-2902) installed on the southeastern corner of Pond 1.

Supplementary Discussion 6. Controlled field test

A controlled field test of ice regeneration was conducted in an open and accessible area (40.461128° N, 86.942524° W) for frequent observation and thickness measurement. A portable refrigerator (Internal dimension 35.0x24.6x20.4 cm, F40C4TMP) with thermal insulation was filled with water and was connected to an external feedback controller to maintain the liquid water temperature at ~2 °C, which is slightly above water's freezing point to demonstrate the localized cooling for ice generation under such unfavored condition. The freezer was kept on a leveled table and the Ice-Wood prototype floated on top of the water. The ice thickness on the Ice-Wood was measured with a caliper. The ice thickness around Ice-Wood, i.e. on the water surface, was measured by drilling a small hole and inserting a short wood shaft connected to a flexible string underneath the ice layer. The distance between the top surface and the wood shaft was marked and subsequently measured by the caliper. This procedure kept minimal disturbance to the ice growth. The ambient conditions were collected every 5 minutes via an online weather channel (Weather Underground) connected to a nearby weather station (KINWESTL83 at 40.46 °N, 86.94 °W). The carbonized wood achieved a temperature elevation of 1.6-4.6 °C via localized solar heating (Fig. S14). The delignified wood exhibited a temperature < 0 °C even when the ambient temperature was approximately 2 °C under direct sunlight, which proved the efficacy of the localized cooling effect.

Supplementary Discussion 7. Coupled heat and mass transport for Ice-Wood optimization

An axisymmetric 2D finite element model is developed in COMSOL Multiphysics® Software 6.0 based on the preliminary configuration of Ice-Wood to study and optimize the design. The coupled heat and mass transport is solved in modules of heat transfer in moist air, moisture transport in air, and laminar flow to represent the Multiphysics of interfacial evaporation, moisture transport, and ice growth in the Ice-Wood. The dimensions of the simulation domains are based on the physical size of the prepared Ice-Wood prototype (Fig. S34). The thickness of air domains above the wood domain top surface and water domain underneath it is four times and twice the wood domain thickness respectively. The width of the air and water domains is set to double of width of the wood domain. It ensures sufficient free space to capture the mixing and vertex in the fluid dynamics simulation. The carbonized wood in the air and the air domain are selected for computation of moisture transport, where the former is assigned as a hygroscopic medium. The Millington and Quirk model is used for effective moisture diffusion coefficient ($D_{v,eff}$).

$$D_{v,eff} = \frac{(1-s_l)\varepsilon_p}{\left[(1-s_l)\varepsilon_p\right]^{-7/3}\varepsilon_p^{\,2}} D_v \tag{11}$$

where D_v is the moisture diffusion coefficient in the free space as 2.42e-5 and 2.19e-5 $m^2\ s^{-1}$ at 20 and 0 °C respectively[23]. s_l and ε_p are liquid water saturation and material's porosity where the numerator of Eq. (11) represents the time-dependent porosity for two-phase flow computation.

The outer boundary of the air domain is set to an open boundary with a zero-pressure constraint at the top right corner for free flow. The interfaces of delignified wood – air and carbonized wood – water are set as wet surfaces with an evaporation rate factor of 2. The umbrella structure is idealized as two boundaries with a thin moisture barrier and non-slip wall boundary conditions to redirect the vapor from interfacial evaporation to the delignified wood. The two phases (vapor and fluid) flow in the porous medium is modeled by varying the phases' relative permeability and the material's porosity based on liquid water saturation according to Ref.[24].

In the heat transfer module, the carbonized wood in the air is a moist porous medium while the rest of the wood main is a porous medium. A phase change material calculation is assigned to the fluid in both free flow region and porous media. The phase change temperature, latent heat, and transition interval are set according to the fluid properties. A similar open boundary BC is assigned to air for free energy flow. The solar heating is included as a constant inward boundary heat flux based on the experimentally measured total solar absorption multiplied a 1000 W m^{-2} solar irradiance. Radiative cooling is assumed as outward boundary heat flux according to the theoretical daytime cooling power.

The materials' thermophysical properties are summarized in Table S2. Air, seawater at 35 salinity, and ice are from the built-in material library of the software. The wood water content (w) is calculated based on the sorption isotherm[25]. The effective water diffusion coefficient ($D_{w,eff}$) in the wood domain is exponentially scaled with its water content, density, and porosity as

$$D_{w,eff} = D_w \exp(-2.8 + 2w/\rho/\varepsilon_p) \tag{12}$$

The ambient temperature and relative humidity are set to 1 °C and 20%. The mesh independence is studied and a relative error of evaporation rate of <0.01% is achieved at 17394 mesh elements (Fig. S35). The corresponding mesh options are the free triangular mesh with an extra fine option calibrated for fluidic dynamics is used for air and Ice-Wood above the water level while an extra fine option for general physics is selected for the remaining domains.

In the study setup, the steady-state velocity field is first solved and then the transient moisture and heat transport is solved for a 30-minute range. The total evaporation rate (kg s^{-1}) is evaluated by the integration of carbonized wood above water level and converted to hourly evaporation flux (kg m^{-2} h^{-1}). The total ice volume or average ice volume fraction in the delignified wood is evaluated by integrating or averaging the ice phase function (0 for the liquid water phase and 1 for the solid ice phase) over the corresponding domains.

The model is validated by simplifying to account only the solar-driven interfacial evaporation and compared to experimentally measured evaporation rate. The time-averaged evaporation rate between 1400 – 1500 s of the experiment and simulation are 0.645 and 0.633 kg m^{-2} h^{-1} respectively. The 1.9% discrepancy between the modeled and measured evaporation rates proves the validity of the major functions and settings of the model. A study of air box size indicates the evaporation rate has been minimally affected by the air box size (Fig. S36). Although the magnitude of the average ice phase increases with air box size, the overall trend remains the same, which supports the qualitative analysis of the design-performance correlation. Then, the full model is used to predict and optimize the Ice-Wood by varying the overall thickness, elevation height of carbonized portions, and area ratio of carbonization (Fig. S17). The area ratio is represented as the nondimensional length of the lateral dimension of carbonized wood over that of the Ice-Wood.

Supplementary Discussion 8. Impact analysis of potential deployment of Ice-Wood

S8.1 Polar sea ice simulation

The open-source code CICE (version 6.4.0) is used to simulate and qualitatively compare the growth and melting of polar sea ice[26]. The model solves the energy and momentum transport equation in the transient state for ice growth and fractional ice coverages given the ambient input data on geographical grids. The sea ice dynamics due to radiative heat exchange, mechanical rafting, and riding are considered. The thermodynamics, ridging, and thickness change of sea ice in the vertical direction to the ocean surface, i.e. column physics, are simulated with a submodule ICEPACK (version 1.3.2)[27]. The model outputs include time series of "grid cell mean ice thickness", "sea surface temperature", and "congelation ice growth rate". The time frame and grid of all simulated cases are 2005 Jan. 1st to 2022 Dec. 31st and 3° displace-pole global grid (gx3). The simulation makes a bold assumption that the ice albedo and ocean albedo are globally and uniformly improved according to the sample's measured spectral data and compares the results to a baseline case for a qualitative assessment. The baseline case uses default input parameters initialized by the code. The modified model parameters for each test case are listed in Table S1. The forcing dataset for ambient data (temperature, total precipitation, downward solar and longwave radiation, *u*- and *v*-component of wind, and specific humidity) is the Japanese 55-year Reanalysis 3-hourly data[28].

Although the current model is preliminary as only the cooling effect and some hydrodynamic merits of Ice-Wood are considered, the comparison proves the efficacy of reversing the trend of ice retreating by deploying the Ice-Wood. The model can be further refined to incorporate the local seeding effect by altering the input parameters of individual cell grids according to the sample properties and performances. Observing the ice dynamics around that cell grid will give a more realistic and quantitative estimation of a global impact. Alternatively, Ice-Wood can also be incorporated in the simulation as snow for their similar thermal conductivity.

S8.2 Carbon sequestration estimation

The application of scalable Ice-Wood in Arctic Ocean contributes to net carbon sequestration in two ways. First, the utilization of natural wood promotes afforestation and active forest management which can be regarded as a carbon sink for Ice-Wood production. Second, the projected increases of equivalent or real old ice area due to the Ice-Wood help improve the overall solar reflectance of the Earth's surface, which can be translated to an equivalent amount of CO_2 drawdown to reach the same forcing. The estimation follows the lab-scale processing of Ice-Wood prototype where the amount of H_2O_2 solution is reduced to 20% of current usage assuming an optimized process. The amount of CO_2 stored by wood or equivalent CO_2 sequestration by change of radiative forcing is estimated with respect to a projected deployment area in the unit of million metric tons CO_{2eq} (MMT CO_{2eq}).

The net carbon sequestration of Ice-Wood production consists of carbon storage by wood utilization and major carbon emission by the production of H_2O_2, acrylic, and LDPE for the delignification and umbrella assembly[29-31]. The carbon storage by wood is estimated as 0.5 kg carbon per kg of wood[32] and converted to CO_2 by the molar mass ratio.

The radiative forcing (dF) is calculated as

$$dF = I_0 (R - R_0) \quad (13)$$

where R and R_0 are the effective and baseline solar reflectance of Earth's surface. I_0 is the annually averaged amount of solar irradiance. R and R_0 are estimated based on the area fraction of total sea ice extent (0.9 solar reflectance) and other surface coverage (0.3 solar reflectance). Then, the CO_2 concentration (C) in ppm can be obtained via[33]

$$dF = 5.35 \ln(C/C_0) \quad (14)$$

where C_0 is the reference CO_2 concentration in the year 1990. The concentration is then converted to MMT CO_{2eq}.

S8.3 Heavy metal detection in leachate

To examine the toxicology of chemicals leaching from the Ice-Wood to the ocean, we tested the heavy metal concentration of the leachate from the water sample collected in the pond field validation test. Water samples of 125 mL were collected 5 cm below the water surface at three random locations in each pond at the beginning and the end of the test with a time interval of 78 days. The leachates of 5 mL after 50 days were tested by Inductively Coupled Plasma Mass Spectrometry (ICP-MS) for As, Cd, Co, Cr, Cu, Mn, Ni, Zn, Fe, and Pd according to possible heavy metals found in wood species[34]. ICP-MS analysis was conducted on a Thermo Scientific Element 2 mass spectrometer equipped with a Teledyne Cetac Aridus II nebulizer. Samples were diluted 5 times to the final solution with 2%HNO_3 and 5 ppb Indium. 5 ppb Indium was used as an internal control. All elements were analyzed under medium resolution. A multi-element standard from Inorganic Venture including 10 ppm of As, Cd, Co, Cr, Cu, Mn, Ni, Zn, Pd, and 1000 ppm of Fe was used.

The concentrations of most tested elements are below the EPA National Recommended Water Quality Criteria - Aquatic Life Criteria[35] or Ref.[36]. Among the test heavy metal elements, concentrations of Cd, Co, Cr, and Fe are below their detection limits (0.06, 0.09, 0.09, and 6.19 μg L^{-1}). In summary, the expected addition of heavy metals from Ice-Wood deployment is within the safety limit and remains minimal harm to the Arctic's ecosystem.

Supplementary Figures

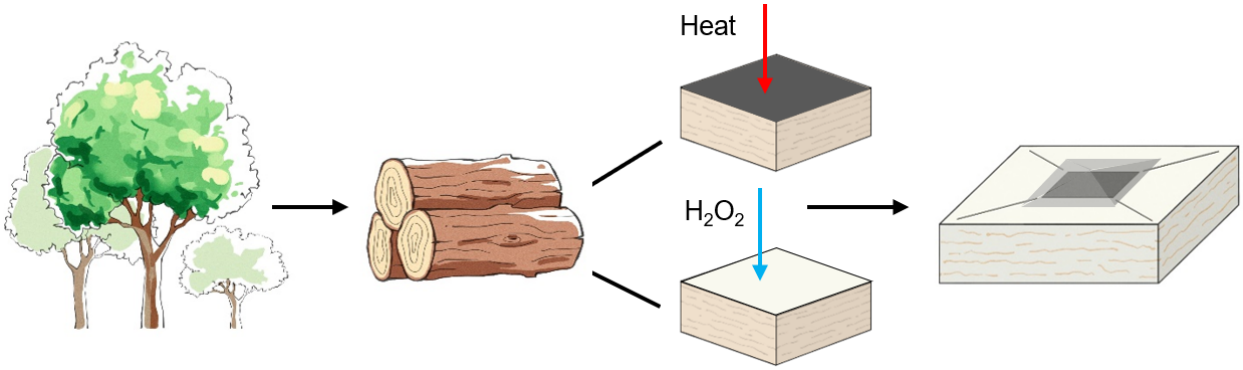

Fig. S1. Schematic of carbonization and delignification toward Ice-Wood assembly.

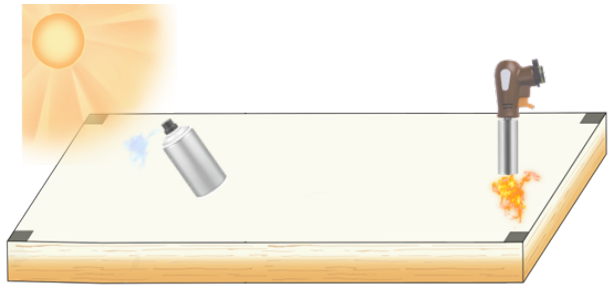

Fig. S2. Schematic of potential large-scale fabrication.

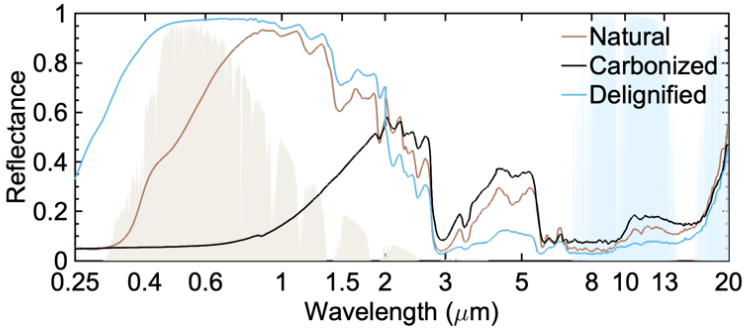

Fig. S3. Reflectance in the UV-VIS-NIR range and IR range for the delignified, carbonized, and natural wood.

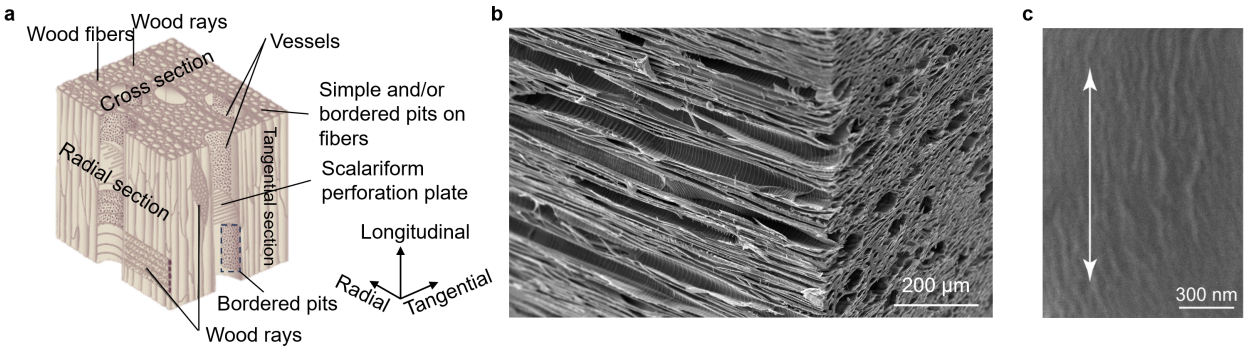

Fig. S4. (a) Nomenclature of hardwood microstructure. SEM showing vessels in cross sections (b) and partially aligned nanofibers (c).

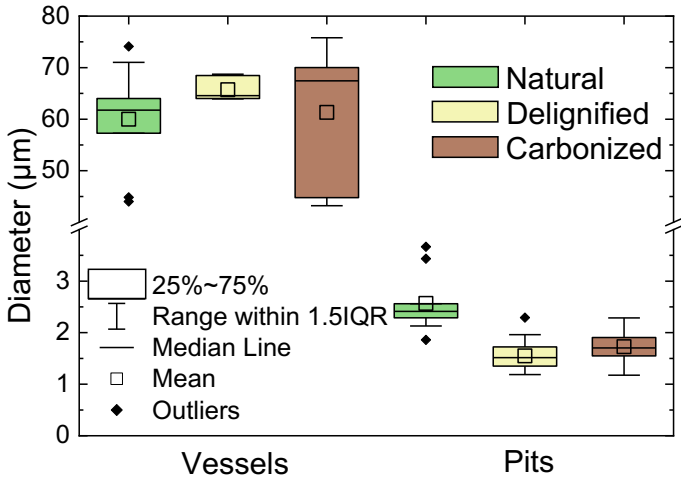

Fig. S5 Effective diameters of vessels and pits in natural, delignified, and carbonized wood derived from SEM (IQR represents interquartile range).

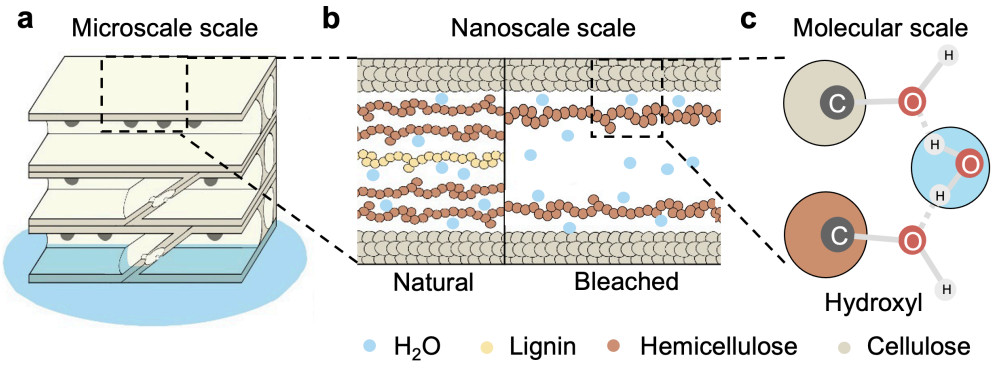

Fig. S6. Schematic of multiscale water transport in hardwood microstructure along the radial direction showing bordered pits.

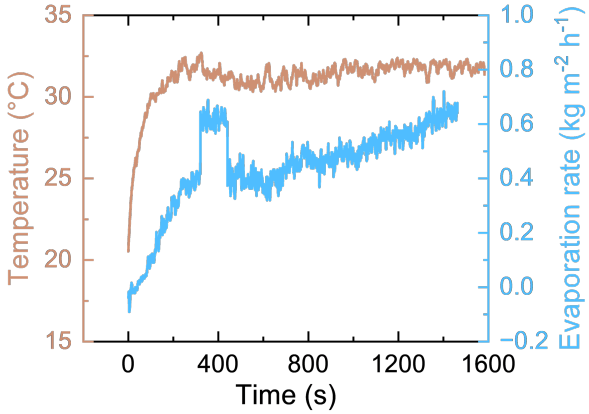

Fig. S7. Temperature and evaporation rate vs. time of solar-driven interfacial evaporation experiment.

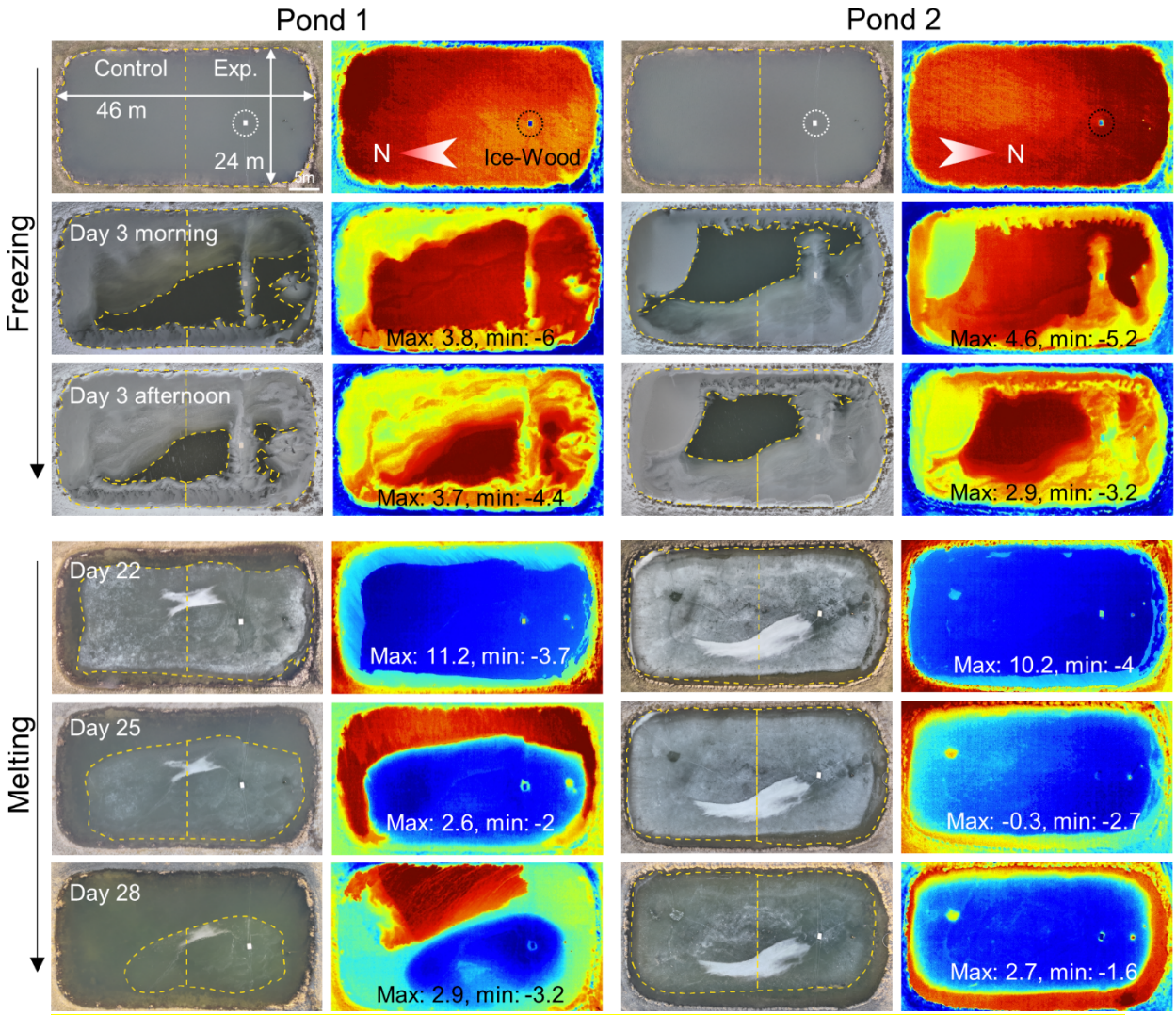

Fig. S8. Digital and IR photos of the two test ponds on an overlook view showing the ice evolution and the temperature distribution.

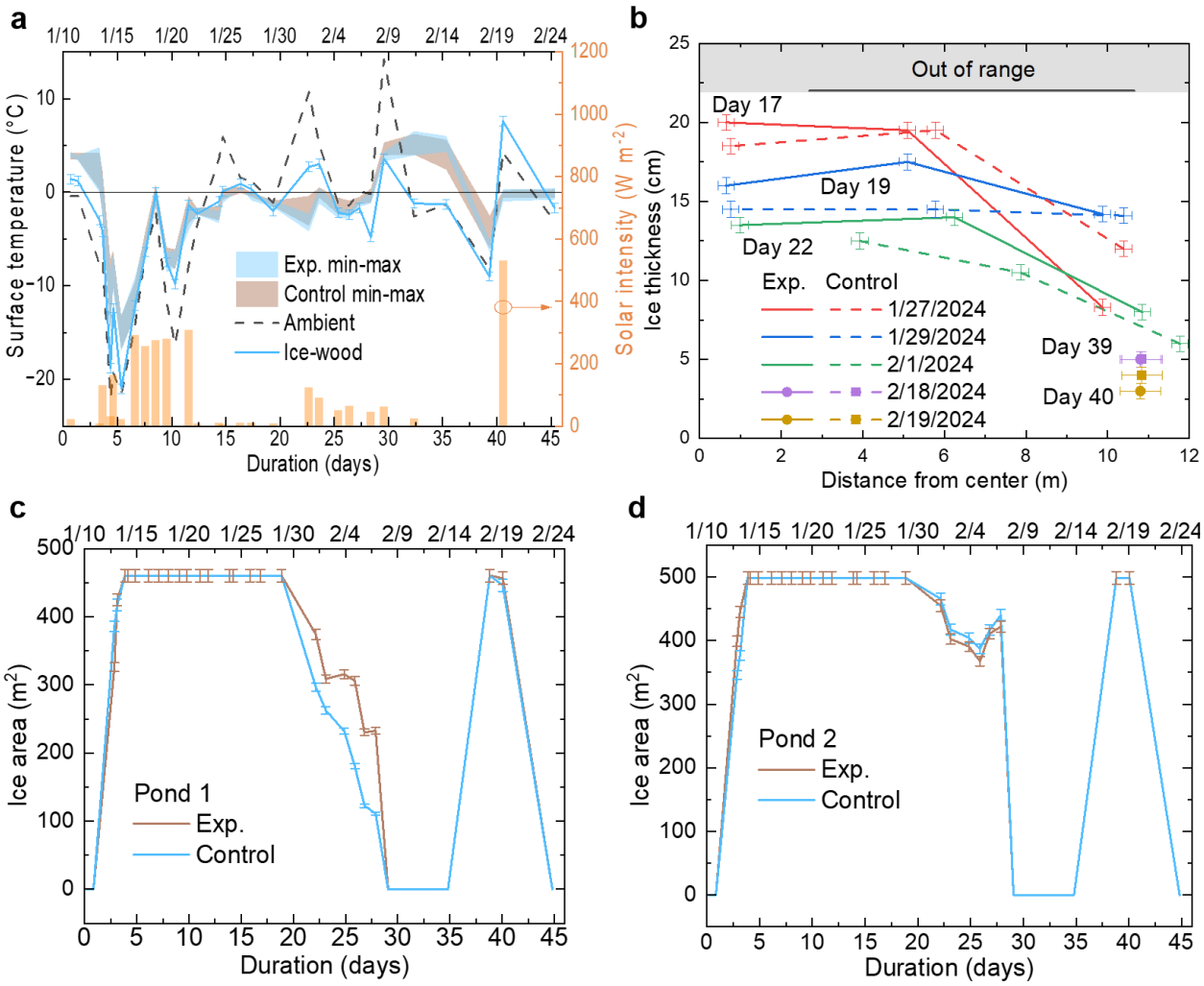

Fig. S9. (a) Pond 2: temperatures of Ice-Wood, max and min of water surface, and ambient on the left y-axis. The right y-axis plots the solar intensity. (b) Pond 2: ice thickness profile vs. distance from the center of the half pond. Ice area evolution during the pond test for Pond 1 (c) and Pond 2 (d).

Fig. S10. Side view of the Ice-Wood during the melting phase in the pond test.

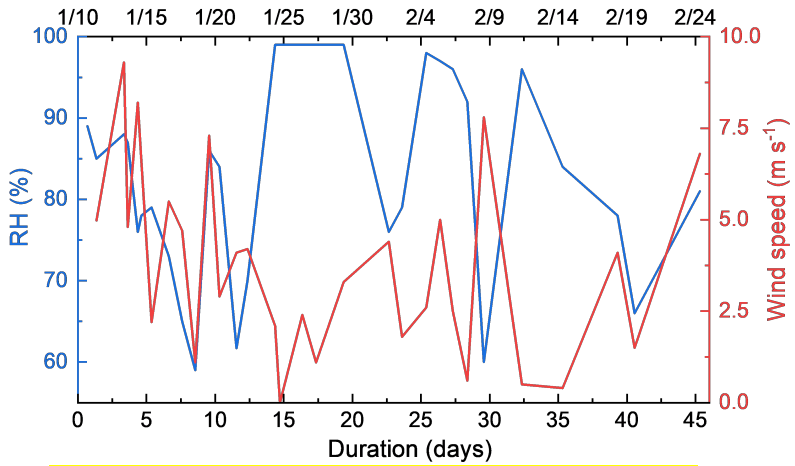

Fig. S11. RH and wind speed during the pond test.

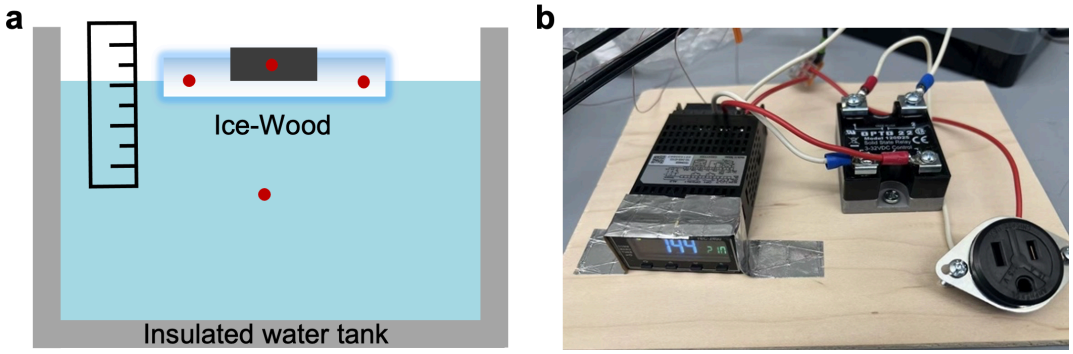

Fig. S12. (a) Schematic of the field test cooling tank. (b) Feedback controller.

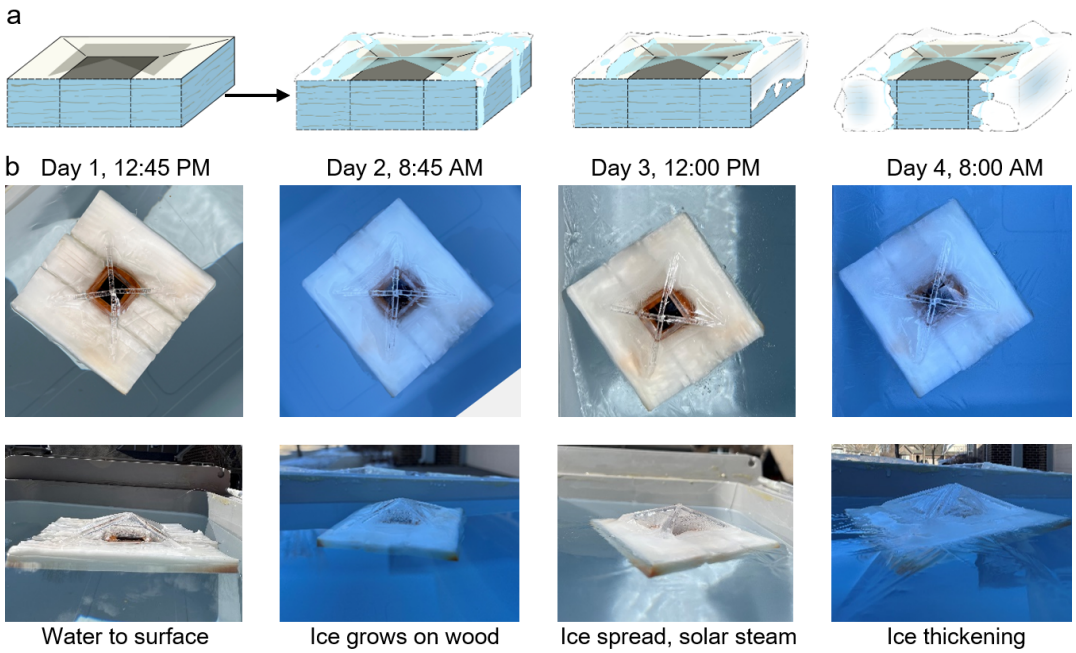

Fig. S13. (a) Schematic of ice regeneration process. (b) Top view and corresponding side view of the Ice-Wood prototype during the field validation March 12th – 15th, 2023.

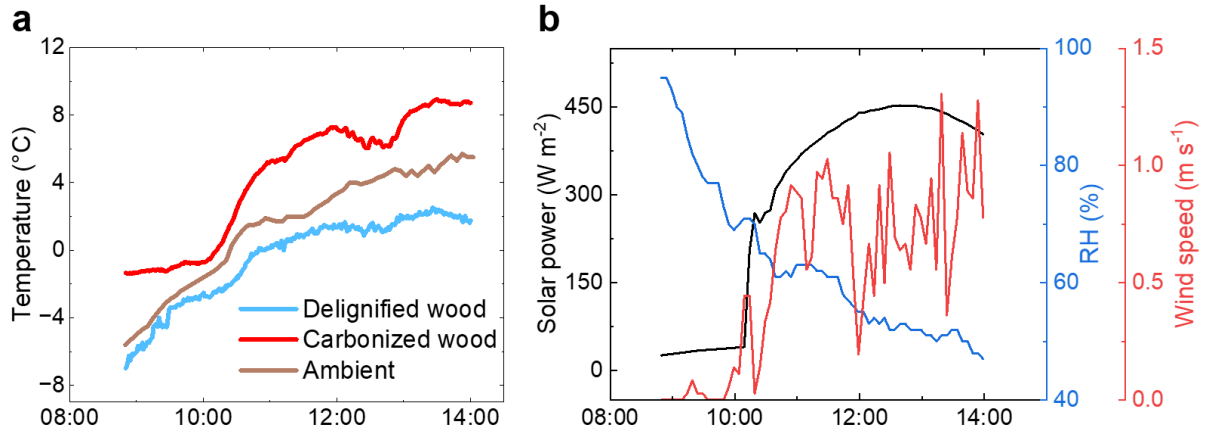

Fig. S14. Temperature profile of delignified wood and carbonized wood (a) and ambient conditions (b) in the field test of Feb. 11th, 2023.

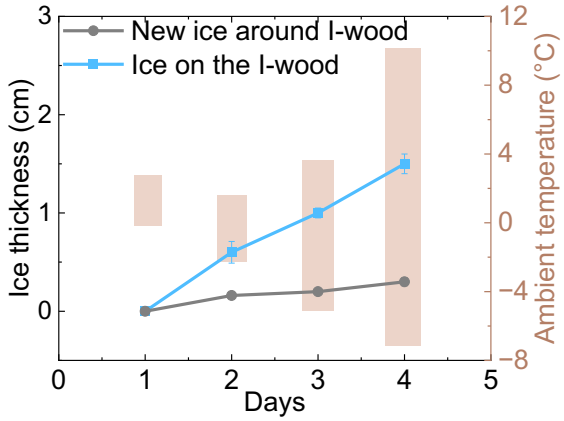

Fig. S15. Temperature profile of delignified wood and carbonized wood in the temperature measurement field test.

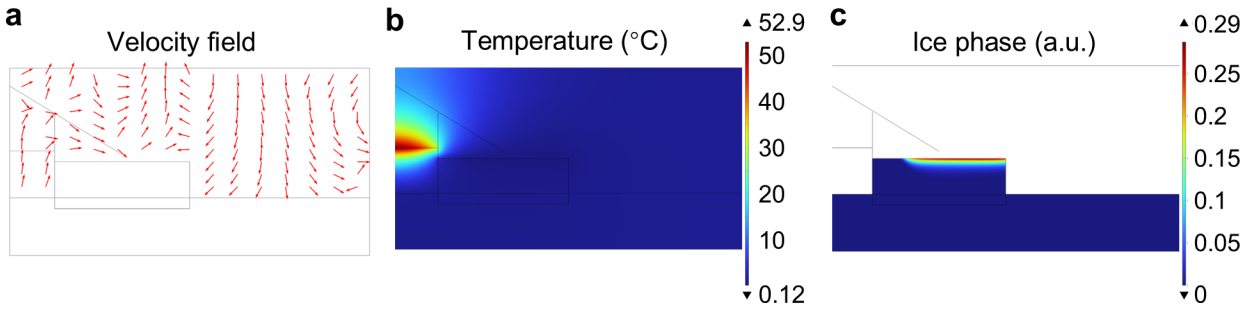

Fig. S16. Simulation results of velocity field (a), ice phase distribution which is dimensionless between 0 and 1 (b), and temperature distribution in °C (c) of Ice-Wood system model.

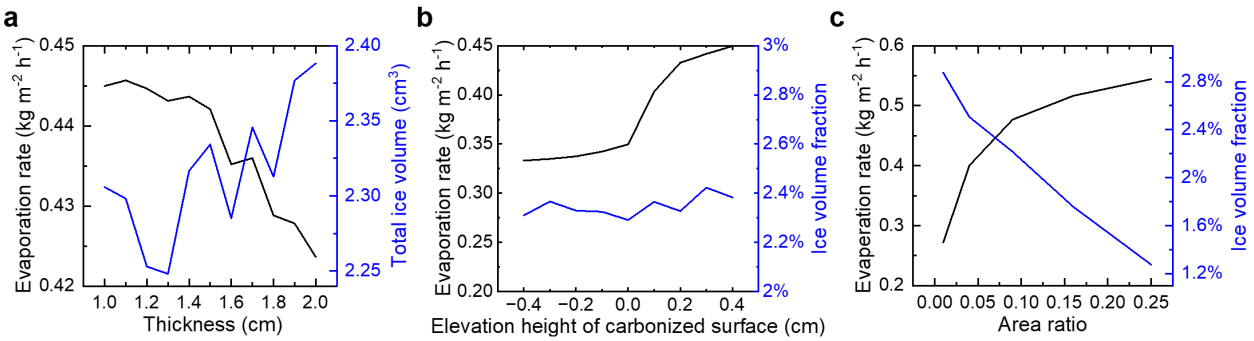

Fig. S17. Evaporation rate and ice volume/volume fraction as a function of overall thickness (a), elevation height of carbonized portion (b), and area ratio of carbonized portion (c) evaluated at 30 min of simulation.

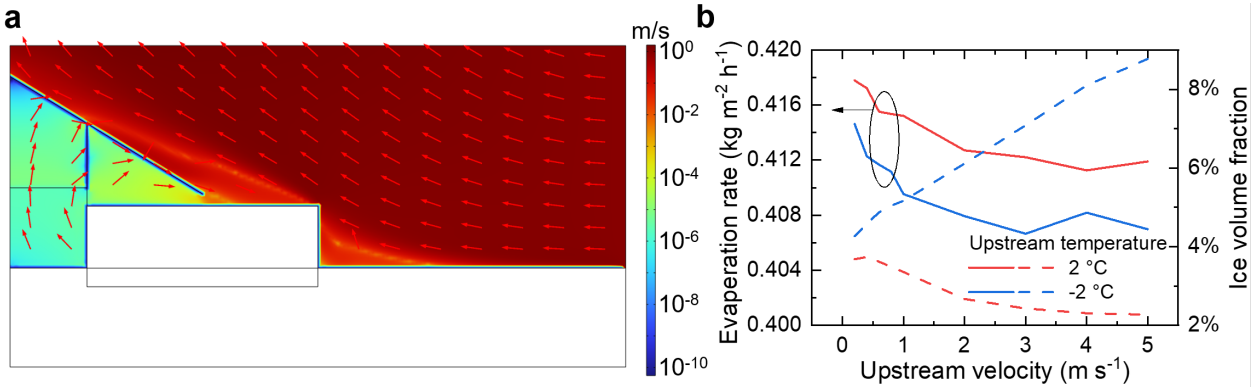

Fig. S18. (a) Flow velocity distribution with field vectors. The color scale is in the log scale with the unit of m s^{-1}. (b) Modeled evaporation rate and average ice phase for different air box sizes.

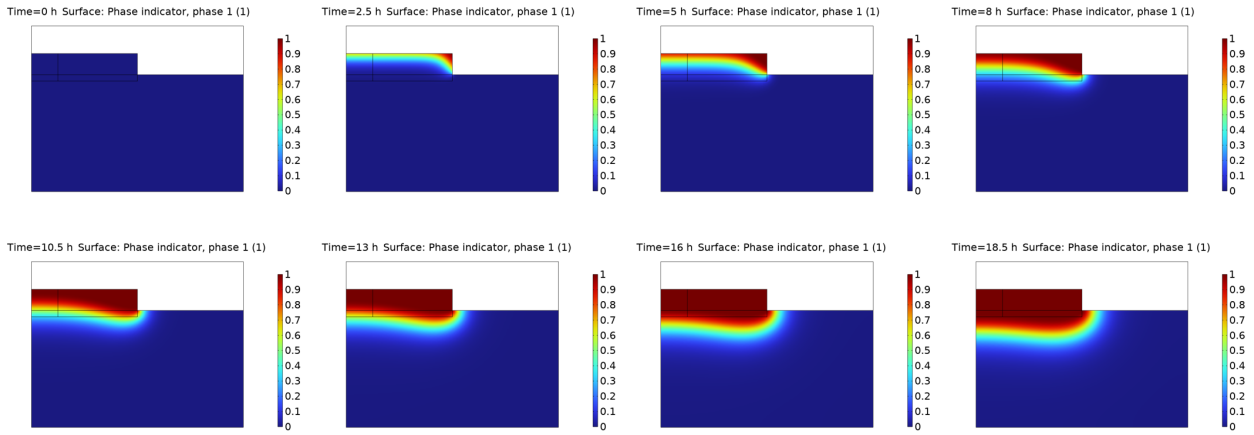

Fig. S19. Evolution of ice phase in 18.5-hour simulation time of partially delignified Ice-Wood. The phase distribution and scale bar represent ice phase as 1 and liquid phase as 0.

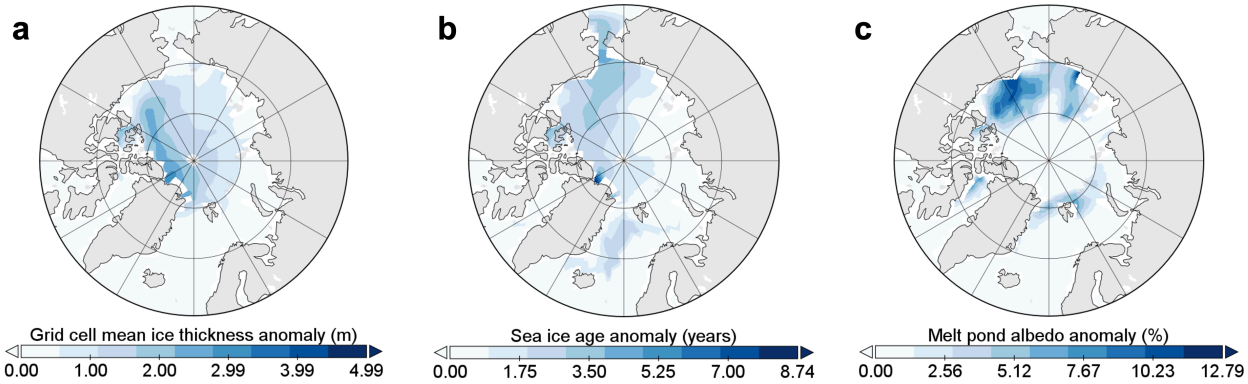

Fig. S20. Anomaly of ice thickness (a), sea ice age (b), and melt pond albedo (c) in Sept. 2022.

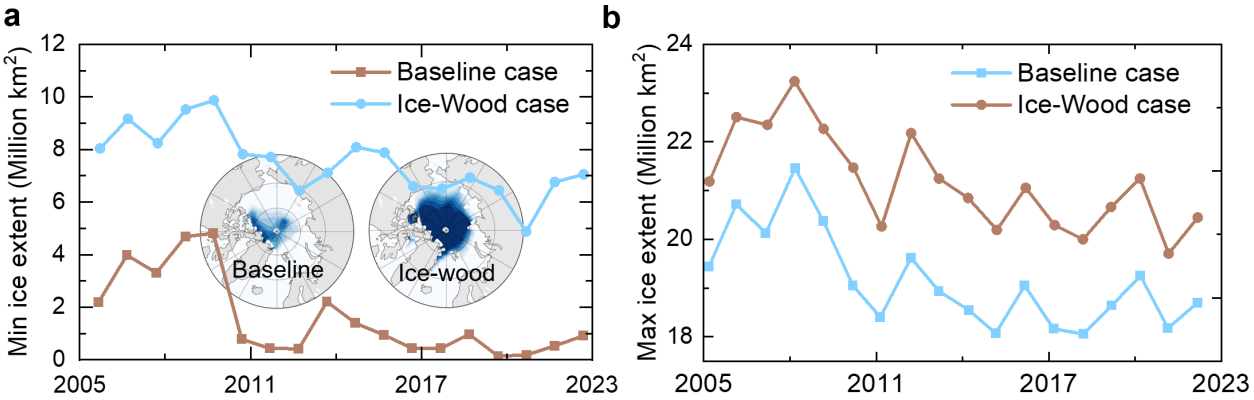

Fig. S21. Minimum (a) and maximum (b) arctic ice extent of each year during 2005-2022 for baseline case and Ice-Wood case. The insets are aggregate ice area of two cases in Sept. 2022. The color bar linearly ranges from 0 to 1.

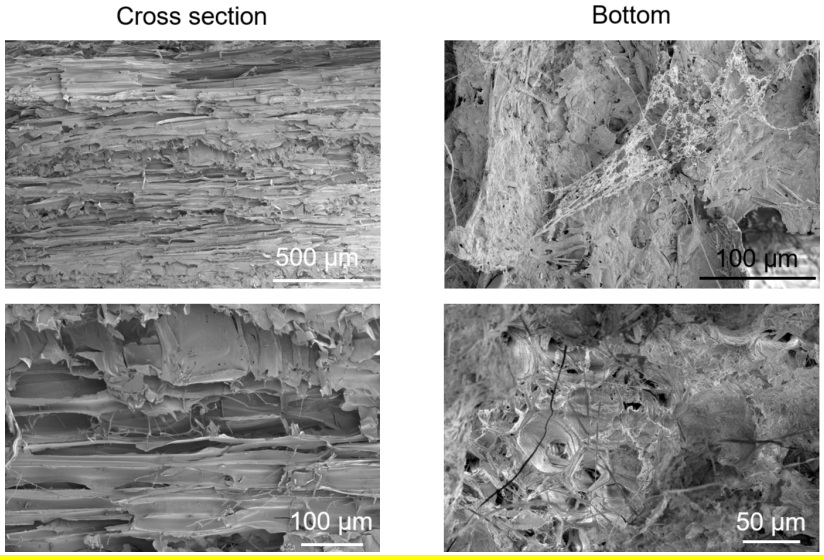

Fig. S22. SEM of Ice-Wood after the pond test at the cross-section and the bottom.

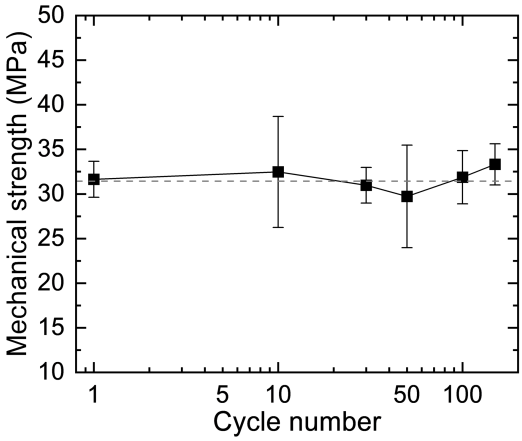

Fig. S23. Mechanical strength of the wood sample after 1, 10, 30, 50, 100, and 150 cycles of freezing and thawing. The dashed line is the mechanical strength of pristine sample, i.e. 0 cycle.

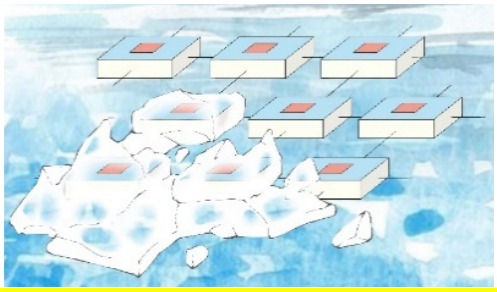

Fig. S24. Schematic illustration of chained Ice-Wood layout in deployment.

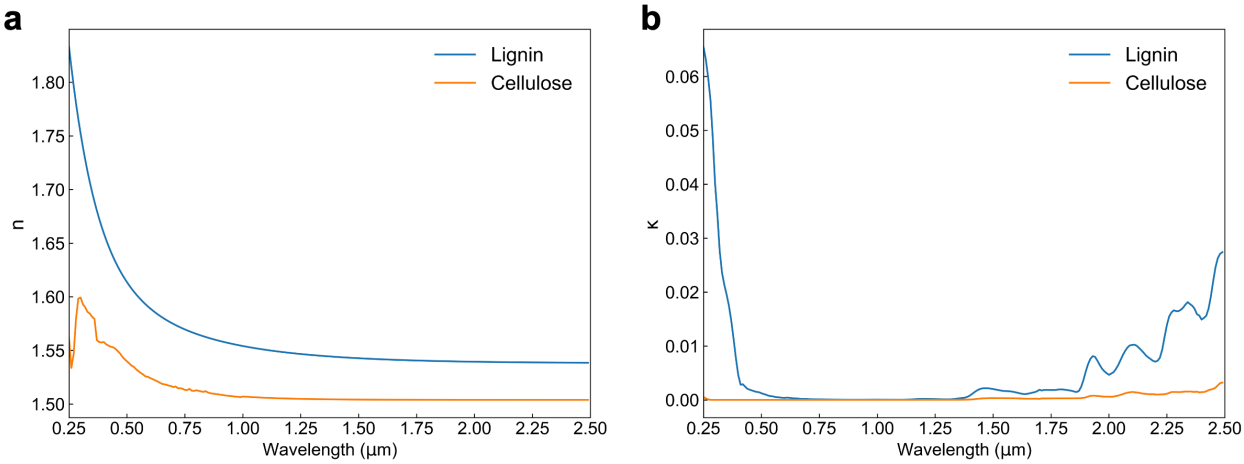

Fig. S25. Refractive index (a) and extinction coefficient (b) of lignin and cellulose.

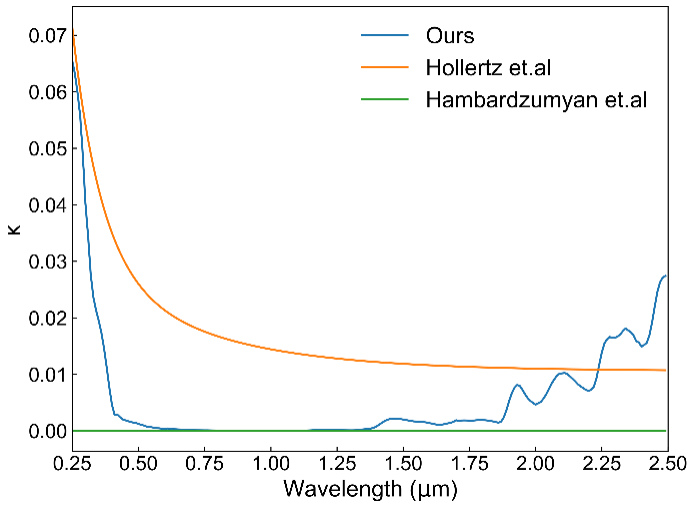

Fig. S26. Comparison of the fitted and literature values[3,8] of lignin's extinction coefficient.

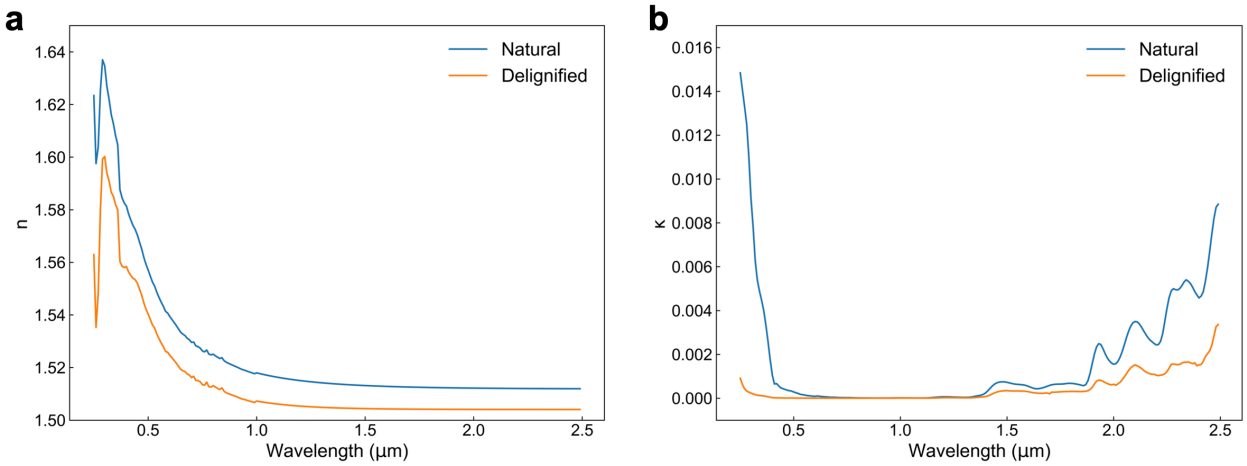

Fig. S27. Effective refractive index (a) and extinction coefficient (b) of natural and delignified wood.

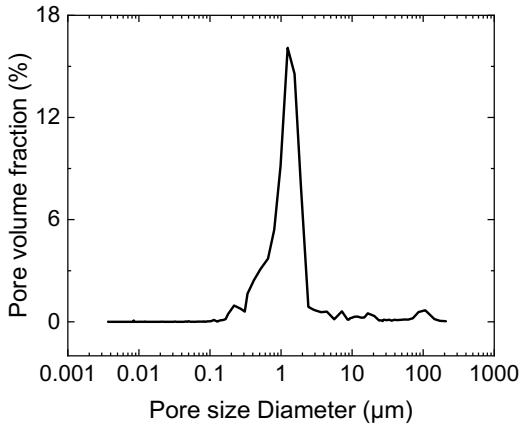

Fig. S28. Pore size distribution of natural wood.

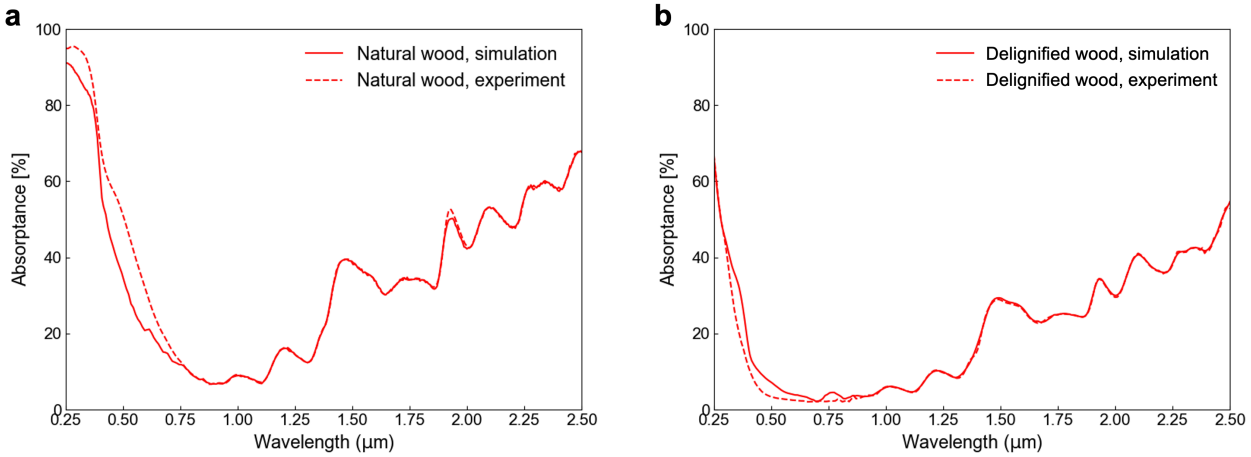

Fig. S29. Simulated and experimental spectral absorptance of natural wood (a) and delignified wood (b).

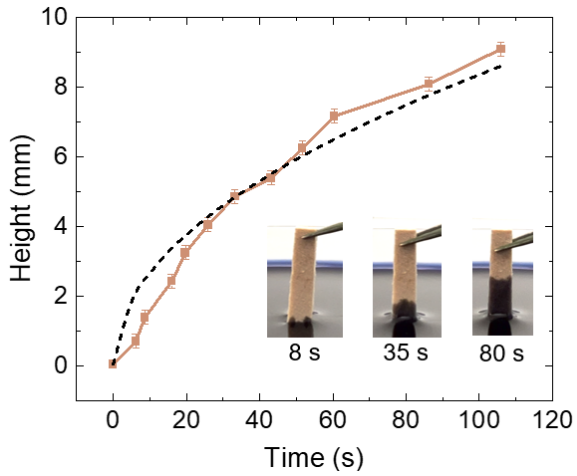

Fig. S30. Capillary height obtained from experiment and fitted with the analytical model along with time. Inset photos are snapshots of the capillary rise experiment.

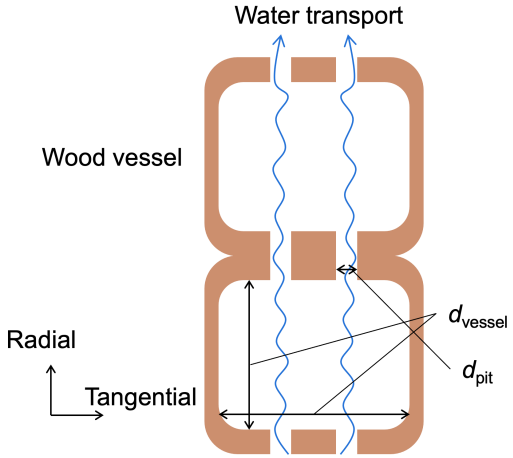

Fig. S31. Schematic of mesoscopic water transport in a conceptualized wood microstructure.

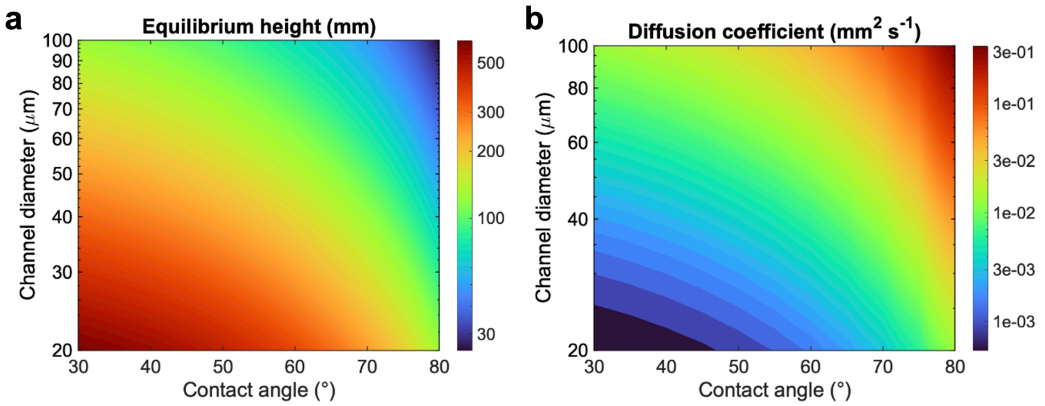

Fig. S32. Analytical solution of equilibrium height (a) and effective diffusion coefficient (b) of radial water transport as a function of vessel diameter and contact angle. The color bars and y-axis are in log scale.

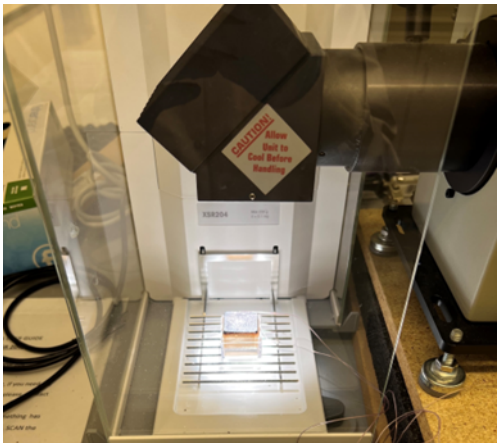

Fig. S33. Photo of solar-driven interfacial evaporation experiment.

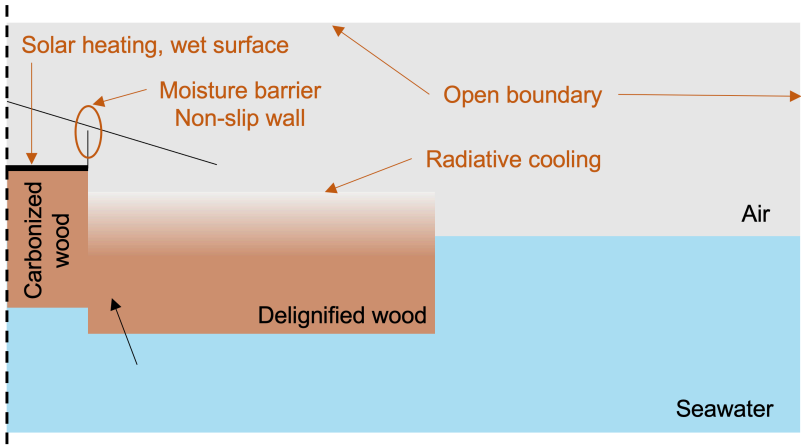

Fig. S34. Annotated axisymmetric 2D modeling domain of coupled heat and mass transport of Ice-Wood.

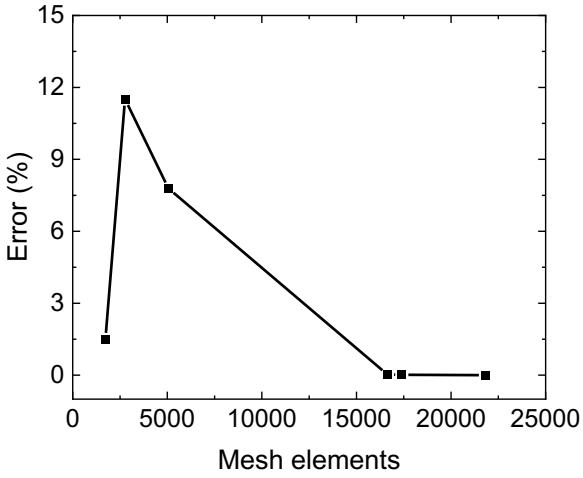

Fig. S35. Relative error of evaporation rate vs. element numbers for mesh independence study.

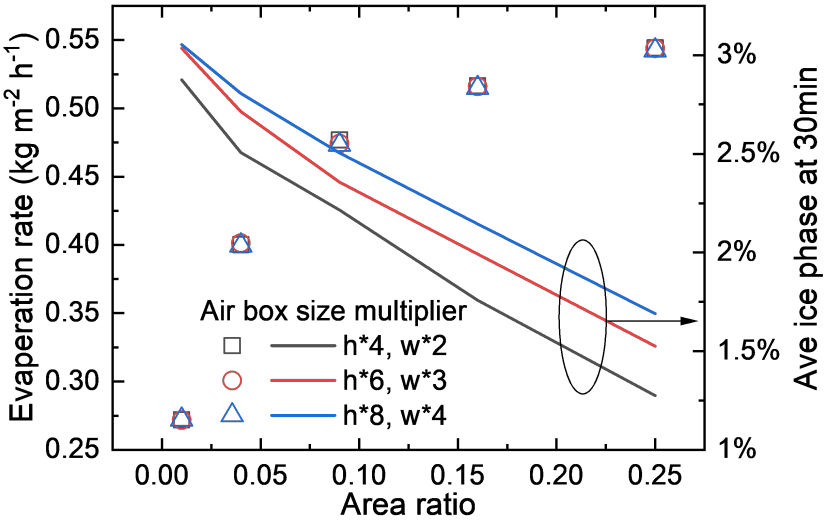

Fig. S36. Modeled evaporation rate and average ice phase for different air box sizes. *h* and *w* are the height and weight of the Ice-Wood domain dimension, and the air box is set to their multiplications.

Supplementary Tables

Table S1. Modified model parameters.

Variables	Baseline	Ice-Wood
Ice visible albedo	0.78	0.967
Ice NIR albedo	0.36	0.920
Ocean albedo	0.06	0.911
Max fraction of melt water added to ponds	1	0.3
Ice thickness threshold for constant albedo (m)	0.3	0.01

Table S2. Material parameters of coupled heat and mass transport in Ice-Wood.

Variable	Value	Ref.
ρ	351.535 (kg m^{-3})	Exp.
$k_{\text{longitudinal}}$	0.38 (W m^{-1} K^{-1}) [a]	Exp.
$k_{\text{tangential/radial}}$	0.22 (W m^{-1} K^{-1}) [a]	Exp.
c_p	1761.194 (J kg^{-1} K^{-1})	Li *et al*.[37]
D_{w}	1.9e-8 (m^2 s^{-1})	Amer *et al*.[21]
ε_{p}	0.768 [b]	Kellogg *et al*.[38]

[a] values after soaking in water. [b] calculated based on the measured bulk density and true density from the reference.

Supplementary References

1 Abdollahi, M. & Hosseini, A. Hydrogen peroxide. *Encyclopedia of toxicology* **3**, 967-970 (2014).

2 Li, Y., Fu, Q., Yu, S., Yan, M. & Berglund, L. Optically transparent wood from a nanoporous cellulosic template: combining functional and structural performance. *Biomacromolecules* **17**, 1358-1364 (2016).

3 Hollertz, R. *et al.* Dielectric properties of lignin and glucomannan as determined by spectroscopic ellipsometry and Lifshitz estimates of non-retarded Hamaker constants. *Cellulose* **20**, 1639-1648 (2013).

4 Bergström, L., Stemme, S., Dahlfors, T., Arwin, H. & Ödberg, L. Spectroscopic ellipsometry characterisation and estimation of the Hamaker constant of cellulose. *Cellulose* **6**, 1-13 (1999).

5 Lahive, C. W., Kamer, P. C., Lancefield, C. S. & Deuss, P. J. An introduction to model compounds of lignin linking motifs; synthesis and selection considerations for reactivity studies. *ChemSusChem* **13**, 4238-4265 (2020).

6 Jaramillo‐Fernandez, J. *et al.* Highly‐scattering cellulose‐based films for radiative cooling. *Advanced Science* **9**, 2104758 (2022).

7 Zhu, W. *et al.* Structurally colored radiative cooling cellulosic films. *Advanced Science* **9**, 2202061 (2022).

8 Hambardzumyan, A. *et al.* Structure and optical properties of plant cell wall bio-inspired materials: cellulose–lignin multilayer nanocomposites. *Comptes rendus biologies* **334**, 839-850 (2011).

9 Markel, V. A. Introduction to the Maxwell Garnett approximation: tutorial. *JOSA A* **33**, 1244-1256 (2016).

10 Li, T. *et al.* A radiative cooling structural material. *Science* **364**, 760-763 (2019).

11 Bohren, C. F. & Huffman, D. R. *Absorption and scattering of light by small particles*. (John Wiley & Sons, 2008).

12 Modest, M. F. in *Radiative Heat Transfer (Third Edition)* (ed Michael F. Modest) 387-439 (Academic Press, 2013).

13 Huang, Z. & Ruan, X. Nanoparticle embedded double-layer coating for daytime radiative cooling. *International journal of heat and mass transfer* **104**, 890-896 (2017).

14 Zhu, W. *et al.* Large-scale industry-compatible sub-ambient radiative cooling pulp. *Cell Reports Physical Science* **3** (2022).

15 Huang, X., Mandal, J., Xu, J. & Raman, A. P. Passive freezing desalination driven by radiative cooling. *Joule* (2022).

16 Segerholm, I. & Claesson, J. Unexpected experimental results for capillary suction in wood: analysis on the fibre level. *Wood Material Science and Engineering* **3**, 109-118 (2008).

17 Zelinka, S. L., Glass, S. V., Boardman, C. R. & Derome, D. Moisture storage and transport properties of preservative treated and untreated southern pine wood. *Wood Material Science & Engineering* **11**, 228-238 (2016).

18 Burridge, H. *et al.* The transport of liquids in softwood: timber as a model porous medium. *Scientific Reports* **9**, 20282 (2019).

19 Rodríguez-Valverde, M. Á. & Miranda, M. T. Derivation of Jurin's law revisited. *European journal of physics* **32**, 49 (2010).

20 Ma, B. Analysis of capillary flow in a parallel microchannel-based wick structure with circular and noncircular geometries. *Langmuir* **36**, 13485-13497 (2020).

21 Amer, M. *et al.* Experimental study of the linear diffusion of water in clonal eucalyptus wood. *International Journal of Thermophysics* **41**, 1-17 (2020).
22 Ma, X. *et al.* High Value Utilization of Waste Wood toward Porous and Lightweight Carbon Monolith with EMI Shielding, Heat Insulation and Mechanical Properties. *Molecules* **28**, 2482 (2023).
23 *Air - Diffusion Coefficients of Gases in Excess of Air.* , <https://www.engineeringtoolbox.com/air-diffusion-coefficient-gas-mixture-temperature-d_2010.html> (2018).
24 Evaporation in Porous Media with Large Evaporation Rates (2023).
25 Hedlin, C. P. *Sorption isotherms of twelve woods at subfreezing temperatures*. (Division of Building Research, National Research Council, 1967).
26 Cice-consortium/cice: CICE Version 6.4.0. (Zenodo, 2022).
27 Cice-consortium/icepack: Icepack 1.3.2. (Zenodo, 2022).
28 Agency/Japan, J. M. (ed Computational and Information Systems Laboratory) (National Center for Atmospheric Research, 2013 updated monthly).
29 Mahmud, M. P. & Farjana, S. H. Comparative eco-profiles of polyethylene terephthalate (PET) and polymethyl methacrylate (PMMA) using life cycle assessment. *Journal of Polymers and the Environment* **29**, 418-428 (2021).
30 Mekes, J. J. *SUSTAINABILITY AND SUPPLY CHAIN CHALLENGES IN HYDROGEN PEROXIDE*, <https://www.hpnow.eu/sustainability-and-supply-chain-challenges-in-hydrogen-peroxide/> (2022).
31 Benavides, P. T., Lee, U. & Zarè-Mehrjerdi, O. Life cycle greenhouse gas emissions and energy use of polylactic acid, bio-derived polyethylene, and fossil-derived polyethylene. *Journal of Cleaner Production* **277**, 124010 (2020).
32 WOODWORKS. *Calculating the Carbon Stored in Wood Products*, <https://www.woodworks.org/resources/calculating-the-carbon-stored-in-wood-products/> (
33 Myhre, G., Highwood, E. J., Shine, K. P. & Stordal, F. New estimates of radiative forcing due to well mixed greenhouse gases. *Geophysical research letters* **25**, 2715-2718 (1998).
34 Pazalja, M. *et al.* Heavy metals content in ashes of wood pellets and the health risk assessment related to their presence in the environment. *Scientific Reports* **11**, 17952 (2021).
35 Agency, U. S. E. P. *National Recommended Water Quality Criteria - Aquatic Life Criteria Table*, <https://www.epa.gov/wqc/national-recommended-water-quality-criteria-aquatic-life-criteria-table> (2023).
36 Barceloux, D. G. & Barceloux, D. Manganese. *Journal of Toxicology: Clinical Toxicology* **37**, 293-307 (1999). https://doi.org:10.1081/CLT-100102427
37 Li, T. *et al.* Scalable and highly efficient mesoporous wood‐based solar steam generation device: localized heat, rapid water transport. *Advanced Functional Materials* **28**, 1707134 (2018).
38 Kellogg, R. M. & Wangaard, F. F. Variation in the cell-wall density of wood. *Wood and Fiber Science*, 180-204 (1969).